Cubic Gyroid Frameworks in Mesostructured Metal Selenides Created from Tetrahedral Zn^{2+}, Cd^{2+}, and In^{3+} Ions and the $[SbSe_4]^{3-}$ Precursor

Nan Ding,[†] Yasuhiro Takabayashi,[‡] Pier Lorenzo Solari,[§] Kosmas Prassides,[‡] Robert J. Pcionek,[†] and Mercouri G. Kanatzidis*[,†]

Department of Chemistry, Michigan State University, East Lansing, Michigan 48824, Department of Chemistry, University of Durham, Durham DH1 3LE, United Kingdom, and European Synchrotron Radiation Facility, 38043 Grenoble Cedex, France

Received April 28, 2006. Revised Manuscript Received June 14, 2006

We describe a new group of well-organized cubic mesostructured metal chalcogenides. They were obtained from the assembly of the tetrahedral $[SbSe_4]^{3-}$ unit and the linking metal ions In^{3+}, Zn^{2+}, and Cd^{2+} in the presence of C*n* ($n = 12, 14, 16$) pyridinium surfactants acting as structure-directing agents. The assembly of the cubic gyroid mesostructure is immediate upon mixing the reactants. The cubic structure, confirmed with X-ray diffraction and transmission electron microscopy, contains an infinitely extended M/Sb/Se network that defines a well-known periodic minimal surface known as the gyroid and possesses an $Ia\bar{3}d$ space group symmetry. The ion In^{3+} is a more versatile linking metal and can also form a hexagonal mesostructure by changing the surfactant concentration or carbon chain length. The pore−pore separations and pore sizes are a function of surfactant chain length in all cases. The cubic mesophases exhibit reversible ion-exchange properties, although the cubic symmetry cannot be retained. All mesophases are mid-gap semiconductor materials with $1.5 < E_g < 2.0$ eV. The nature of the Sb/Se species in the structure was probed with X-ray absorption near edge structure (XANES) measurements at the Sb L^{III} edge. We observe an evolution in the spectra that is consistent with an increased proportion of the reduced $[Sb^{III}Se_3]^{3-}$ species at the expense of precursor $[Sb^{V}Se_4]^{3-}$ as the Lewis acidity of the metal ions increases along the series Zn^{2+}, Cd^{2+}, and In^{3+}, and this is in agreement with the Raman spectroscopic results which are also reported.

Introduction

Mesostructured chalcogenides with periodic porous frameworks have the potential to achieve a set of properties that are normally encountered in disparate materials, for example, mesostructured silicas and chalcogenide semiconductors. Unlike the mesostructured silicas[1] which form from the self-polymerization of silicates, the chalcogenides are typically assembled via coordination reactions between two different precursors,[2] namely a building cluster anion and a linking metal cation. So far, the most studied building blocks are the tetrahedral $[MQ_4]^{4-}$,[3,4] $[M_4Q_{10}]^{4-}$ [2,5,6] (M = Ge, Sn; Q = S, Se, Te), and the dimeric $[Sn_2Q_6]^{4-}$ (Q = S,[7] Se[8]) units which in most cases give a hexagonal structure consisting of honeycomb arrays of parallel pore tunnels.[9] A rarer yet more interesting structure is the cubic MCM-48 type, which possesses a gyroid surface with a three-dimensional (3D) pore network. For this reason it is supposed to be a superior host for guest diffusion.[9−11] The gyroid is a fascinating triply periodic minimal surface that divides all of space into two congruent regions, and it has been of general scientific interest.[12] The two interpenetrating regions of labyrinthine

[†] Michigan State University.
[‡] University of Durham.
[§] European Synchrotron Radiation Facility.

(1) (a) Beck, J. S.; Vartuli, J. C.; Roth, W. J.; Leonowicz, M. E.; Kresge, C. T.; Schmitt, K. D.; Chu, C. T.-W.; Olson, D. H.; Sheppard, E. W.; McCullen, S. B.; Higgins, J. B.; Schlenker, J. L. *J. Am. Chem. Soc.* **1992**, *114*, 10834. (b) Huo, Q.; Margolese, D. I.; Ciesla, U.; Feng, P.; Gier, T. E.; Sieger, P.; Leon, R.; Petroff, P. M.; Schuth, F.; Stucky, G. D. *Nature* **1994**, *368*, 317. (c) Tanev, P. T.; Pinnavaia, T. J. *Science* **1995**, *267*, 865. (d) Prouzet, E.; Pinnavaia, T. J. *Angew. Chem., Int. Ed. Engl.* **1997**, *36*, 516. (e) Zhao, D.; Feng, J.; Huo, Q.; Melosh, N.; Fredrickson, G. H.; Chmelka, B. F.; Stucky, G. D. *Science* **1998**, *279*, 548. (f) Asefa, T.; Kruk, M.; MacLachlan, M. J.; Coombs, N.; Grondey, H.; Jaroniec, M.; Ozin, G. A. *J. Am. Chem. Soc.* **2001**, *123*, 8520. (g) Kim, T.-W.; Kleitz, F.; Paul, B.; Ryoo, R. *J. Am. Chem. Soc.* **2005**, *127*, 7601. (h) Lettow, J. S.; Han, Y.; Schmidt-Winkel, P.; Yang, P.; Zhao, D.; Stucky, G. D.; Ying, J. Y. *Langmuir* **2000**, *16*, 8291. (i) Sayari, A.; Hamoudi, S. *Chem. Mater.* **2001**, *13*, 3151.
(2) Trikalitis, P. N.; Rangan, K. K.; Kanatzidis, M. G. *J. Am. Chem. Soc.* **2002**, *124*, 2604.
(3) (a) Trikalitis, P. N.; Rangan, K. K.; Bakas, T.; Kanatzidis, M. G. *Nature* **2001**, *410*, 671. (b) Trikalitis, P. N.; Bakas, T.; Kanatzidis, M. G. *J. Am. Chem. Soc.* **2005**, *127*, 3910.
(4) Riley, A. E.; Tolbert, S. H. *J. Am. Chem. Soc.* **2003**, *125*, 4551.
(5) (a) MacLachlan, M. J.; Coombs, N.; Ozin, G. A. *Nature* **1999**, *397*, 681. (b) MacLachlan, M. J.; Coombs, N.; Bedard, R. L.; White, S.; Thompson, L. K.; Ozin, G. A. *J. Am. Chem. Soc.* **1999**, *121*, 12005.
(6) (a) Wachhold, M.; Rangan, K. K.; Lei, M.; Thorpe, M. F.; Billinge, S. J. L.; Petkov, V.; Heising, J.; Kanatzidis, M. G. *J. Solid State Chem.* **2000**, *152*, 21. (b) Wachhold, M.; Rangan, K. K.; Billinge, S. J. L.; Petkov, V.; Heising, J.; Kanatzidis, M. G. *Adv. Mater.* **2000**, *12*, 85. (c) Rangan, K. K.; Trikalitis, P. N.; Bakas, T.; Kanatzidis, M. G. *Chem. Commun.* **2001**, 809. (d) Rangan, K. K.; Billinge, S. J. L.; Petkov, V.; Heising, J.; Kanatzidis, M. G. *Chem. Mater.* **1999**, *11*, 2629.
(7) Rangan, K. K.; Trikalitis, P. N.; Canlas, C.; Bakas, T.; Weliky, D. P.; Kanatzidis, M. G. *Nano Lett.* **2002**, *2*, 513.
(8) Trikalitis, P. N.; Rangan, K. K.; Bakas, T.; Kanatzidis, M. G. *J. Am. Chem. Soc.* **2002**, *124*, 12255.
(9) (a) Kresge, C. T.; Leonowicz, M. E.; Roth, W. J.; Vartuli, J. C.; Beck, J. S. *Nature* **1992**, *359*, 710. (b) Xia, Y.; Mokaya, R. *J. Mater. Chem.* **2003**, *13*, 657. (c) Petitto, C.; Galarneau, A.; Driole, M.-F.; Chiche, B.; Alonso, B.; Di Renzo, F.; Fajula, F. *Chem. Mater.* **2005**, *17*, 2120.

10.1021/cm0609956 CCC: $33.50
Published on Web 08/24/2006

character do not cross, so a mobile species in one region cannot cross over to the other. The occurrence, nature, and properties of the gyroid surface are of broad scientific interest.[8,9] Cubic mesophases with a gyroid framework, however, are difficult to achieve both in silicas[11] and in chalcogenides,[8] mainly because of the very specific set of synthetic conditions that need to be met for their stabilization. These conditions involve not only proper temperatures and concentrations but also specific combinations of reactants that present suitable geometric and charge-matching fits between surfactant, precursors, and linking agent. In general, the correct set of combinations likely to give the cubic structure is difficult to predict. In the family of mesostructured chalcogenides, there are only two examples possessing MCM-48 symmetry: the $Zn^{2+}/[SnSe_4]^{4-}$-based *c*-C_{16}PyZnSnSe[3a] and $Pt^{2+}/[Sn_2Se_6]^{4-}$-based *c*-C_nPyPtSnSe[8] ($n = 18, 20$), both requiring formamide solvent to form. The combination of building blocks with square planar linking topologies, that is, Pt^{2+} and $[Sn_2Se_6]^{4-}$, leads readily to mesostructures with MCM-48 type symmetry.[8]

In this work, we report a new inorganic framework system that adopts the gyroid cubic porous structure, and it is based on the aqueous chemistry of the tetrahedral anion $[SbSe_4]^{3-}$ and the linking metal cations In^{3+}, Zn^{2+}, and Cd^{2+} templated by long chain alkyl pyridinium surfactants $C_nH_{2n+1}Py^+$ (C_nPy, $n = 14, 16$). The discovery of stable cubic phases *c*-C_nPyMSbSe starting with $[SbSe_4]^{3-}$, an anion with a different size, shape, and charge than $[Sn_2Se_6]$,$^{4-}$ and of linking metal centers with tetrahedral rather than square planar coordination geometry implies a wider occurrence and scope of this type of structure than originally expected. This realization could help to expand the class of gyroid surface structures and lead to a broad set of semiconducting mesoporous materials with this intriguing geometrical motif.

Experimental Section

Syntheses. *Starting Materials.* K_3SbSe_4 was synthesized by direct combination of K_2Se, Sb, and Se in a 13 mm quartz tube, which was flame-sealed under vacuum and heated at ~900 °C. The purity of the starting K_3SbSe_4 was confirmed by powder X-ray diffraction (XRD) and Raman experiments. Cetylpyridinium bromide monohydrate (C_{16}PyBr·H_2O) was purchased from Aldrich. The other surfactants were synthesized by reacting the corresponding alkyl bromide with excess pyridine in ethanol under reflux conditions. $CHCl_3$−ethyl acetate was used to purify the compounds. $InCl_3$, $ZnCl_2$, and $CdCl_2$ were purchased from Cerac, Spectrum, and Mallinckrodt.

Hexagonal Indium Antimony Selenide h-C_{14}PyInSbSe. An amount of 0.277 g of K_3SbSe_4 (0.5 mmol) was dissolved in 10 mL of water upon stirring and heating at 80 °C. An orange solution formed quickly, and 2.0 g of C_{14}PyBr (5.6 mmol) was then added as a solid into the solution and stirred for about 20 min, forming a clear dark red solution. An amount of 0.055 g of $InCl_3$ (0.25 mmol) was then dissolved in 3 mL of water in another flask and added into the C_{14}Py/$SbSe_4$/H_2O mixture dropwise within 5 min. An orange precipitate formed immediately. After the entire $InCl_3$ solution was added, the reaction mixture was stirred overnight at 80 °C. The product was isolated by filtration, washed with warm water and dried under vacuum. The yield was ~75% based on K_3SbSe_4.

Hexagonal Indium Antimony Selenide h-C_{16}PyInSbSe. The procedure and amounts used to prepare this material were almost identical to those of *h*-C_{14}PyInSbSe given above, except that C_{16}PyBr·H_2O and 20 mL of water (to form the C_{16}Py/$SbSe_4$/H_2O mixture) were used instead. The yield was ~54% based on K_3SbSe_4.

Cubic Indium Antimony Selenide c-C_{16}PyInSbSe. An amount of 0.277 g of K_3SbSe_4 (0.5 mmol) was dissolved in 10 mL of water upon stirring and heating at 80 °C. An orange solution formed quickly, and 2.0 g C_{16}PyBr·H_2O (5.2 mmol) was then added as a solid into the solution and stirred for about 20 min, forming a clear dark red solution. An amount of 0.055 g of $InCl_3$ (0.25 mmol) was then dissolved in 3 mL of water in another flask and added into the C_{16}Py/$SbSe_4$/H_2O dropwise within 5 min. A dark red precipitate formed immediately. However, the reaction mixture was stirred overnight at 80 °C. The product was isolated by filtration, washed with warm water and dried under vacuum. The yield was ~57% based on K_3SbSe_4.

Cubic Zinc/Cadmium Antimony Selenide c-C_nPyMSbSe (M = Zn, Cd; n = 14, 16). The procedure and amounts used to prepare this material were almost identical to those of *c*-C_{16}PyInSbSe given above, except that C_nPyBr was dissolved into 20 mL of water first, and then K_3SbSe_4/H_2O and MCl_2/H_2O (in 3 mL of H_2O, respectively) were added into C_nPyBr/H_2O simultaneously. Doubling the amount of the surfactant did not affect the quality of the product as judged by appearance and XRD. The yields for all these compounds were ~70% based on K_3SbSe_4.

In all syntheses above, the filtrate was red/orange.

Ion-Exchange Reactions. Ion-exchange reactions between C_{12}PyBr and *h*/*c*-C_nPyMSbSe were performed in a nitrogen atmosphere at room temperature. Generally, an amount of 0.5 g of C_{12}PyBr was dissolved in 5 mL of water, and to the surfactant solution was added ~40 mg of *h*/*c*-C_nPyMSbSe. The mixture was stirred overnight, and the solid was isolated by filtration, washed with warm water and dried under vacuum. No obvious color change was observed after the ion-exchange experiment.

Physical Measurements. Powder XRD patterns were acquired on a calibrated Rigaku Rotaflex diffractometer (45 kV, 100 mA) using a rotating anode Cu Kα radiation source. The scan rates were between 0.10 and 0.20°/min and had a step size of 0.04°.

Quantitative microprobe analyses were performed on a JEOL JSM-6400V scanning electron microscope (SEM) equipped with a Noran energy dispersive spectroscopy (EDS) detector. Data acquisition was performed with an accelerating voltage of 20 kV and a 60 s accumulation time.

Elemental C, H, and N analyses were obtained on a Perkin-Elmer Series II CHNS/O analyzer 2400.

(10) (a) Jain, A.; Toombes, G. E. S.; Hall, L. M.; Mahajan, S.; Garcia, C. B. W.; Probst, W.; Gruner, S. M.; Wiesner, U. *Angew. Chem.* **2005**, *117*, 1252. (b) Schumacher, K.; Ravikovitch, P. I.; Chesne, A. D.; Neimark, A. V.; Unger, K. K. *Langmuir* **2000**, *16*, 4648. (c) Gandy, P. J. F.; Klinowski, J. *Chem. Phys. Lett.* **2000**, *321*, 363. (d) Schoen, A. *Infinite periodic minimal surfaces without self-intersections*; NASA Technical Note, D-5541; NASA: Washington, DC, 1970. (e) Grosse-Brauckmann, K. *Exp. Math.* **1997**, *6*, 33. (f) Harting, J.; Harvey, M.; Chin, J.; Conveney, P. *Comput. Phys. Commun.* **2004**, *165*, 97. (g) Fogden, A.; Haeberlein, M.; Lidin, S. *J. Phys. I (France)* **1993**, *3*, 2371.

(11) (a) Hyde, S. T.; Ninham, B.; Andersson, S.; Blum, Z.; Landh, T.; Larsson, K.; Lidin, S. *The Language of Shape*; Elsevier: Amsterdam, 1997. (b) Lee, S.; Mallik, A. B.; Xu, Z.; Lobkovsky, E. B.; Tran, L. *Acc. Chem. Res.* **2005**, *38*, 251. (c) Huo, Q.; Leon, R.; Petroff, P. M.; Stucky, G. D. *Science* **1995**, *268*, 1324. (d) Alfredsson, V.; Anderson, M. W.; Ohsuna, T.; Terasaki, O.; Jacob, M.; Bojrup, M. *Chem. Mater.* **1997**, *9*, 2066. (e) Kim, J. M.; Kim, S. K.; Ryoo, R. *Chem. Commun.* **1998**, 259. (f) Sayari, A. *J. Am. Chem. Soc.* **2000**, *122*, 6504.

(12) (a) Xia, Y.; Mokaya, R. *Microporous Mesoporous Mater.* **2004**, *68*, 1. (b) Nishiyama, N.; Koide, A.; Egashira, Y.; Ueyama, K. *Chem. Commun.* **1998**, 2147. (c) Alfredsson, V.; Anderson, M. W. *Chem. Mater.* **1996**, *8*, 1141.

Thermogravimetric analyses (TGA) were performed using a computer controlled Shimadzu TGA-50 thermal analyzer. Typically, 20 mg of sample was placed in a silica bucket and heated in a nitrogen flow of 70 mL/min with a rate of 10 °C/min.

UV/vis/near-IR diffuse reflectance spectra were obtained at room temperature on a Shimadzu UV-3101PC double-beam, double monochromator spectrophotometer in the wavelength range of 200−2500 nm. $BaSO_4$ powder was used as a reference (100% reflectance) and base material on which the powder sample was coated. Reflectance data were converted to absorbance data as described elsewhere.[13]

Raman spectra (3500−100 cm^{-1}) were recorded on a computer-controlled BIO-RAD Fourier transform (FT)−Raman spectrometer with a Spectra-Physics Topaz T10-106c 1064-nm YAG laser. The instrument was configured in 180° backscattering mode, and the samples were loaded into melting point capillary tubes.

High-resolution transmission electron microscopy (TEM) micrographs were obtained with a JEOL 120CX instrument equipped with CeB_6 filament and operating at 120 kV. The samples were gently ground and suspended in ethyl ether in a glovebox. A holey carbon grid was dipped into the suspension and dried in the air prior to the TEM experiments.

X-ray absorption near edge structure (XANES) measurements were performed at ambient temperature at the Sb L_{III} edge with the spectrometer on beamline BM29 at the European Synchrotron Radiation Facility, Grenoble, France. Spectra were collected from 13-mm diameter pellets, made from powdered samples and graphite, in transmission mode using a Si(111) monochromator, and the energy was calibrated using Sn foil.

Results and Disscussion

The combination of a variety of chalcogenide anions with linking metals in the presence of structure-directing agents such as long hydrocarbon chain surfactants is expected to lead to mesophases; however, the resultant structure type cannot be predicted a priori. When the hydrocarbon chain surfactants are cations and the inorganic structure has a net negative charge, five possibilities exist for the overall structure and pore organization. These are disordered wormhole,[6a] hexagonal,[2−5] stabilized lamellar,[14] cubic, and lamellar.[15] The latter in fact has only two-dimensional galleries. The rarest architecture is the cubic one. We were, therefore, surprised to observe that in the case of the tetrahedral transition metal ions Zn^{2+}, Cd^{2+}, and In^{3+} and the $[SbSe_4]^{3-}$, the reaction chemistry readily led to cubic symmetry which is associated with the gyroid surface. This structure was the most stable and formed in every case as long as the surfactant was $C_{14}Py^+$ and $C_{16}Py^+$.

The assembly of these cubic mesophases requires $[SbSe_4]^{3-}$ as the precursor anion and water as the solvent:

$$C_nPy^+ + M^{m+} + [SbSe_4]^{3-} \xrightarrow{H_2O,\ \sim 80°C} c\text{-}C_nPyMSbSe$$

($n = 16$ when $M^{m+} = In^{3+}$; $n = 14, 16$ when $M^{m+} = Zn^{2+}$, Cd^{2+}). This is the first example we are aware of that shows ordered cubic mesostructured chalcogenides forming in water. Interestingly, the use of $[SbSe_3]^{3-}$ as the precursor anion (a Sb^{3+} species) did not lead to ordered mesostructures. Instead, highly disordered C_nPyMSbSe materials were obtained with a wormhole-type pore arrangement.

The In^{3+} ion exhibited a more versatile behavior as a linker in this system compared to Zn^{2+} and Cd^{2+}, as it was more responsive to changes in conditions. Halving the concentration of the $C_{16}Py/SbSe_4/H_2O$ solution or reducing the surfactant carbon chain length to C14 both caused the cubic indium antimony selenide to change to a hexagonal form (*h*-C_nPyInSbSe, $n = 14, 16$). In contrast, the corresponding reactions with Zn^{2+} and Cd^{2+} were not influenced by these changes. All reactions have a relatively narrow temperature range between 75 and 85 °C to yield ordered mesostructure. Above this range, a disordered wormhole mesostructure was generally produced.

Powder XRD patterns of the hexagonal and cubic compounds are shown in Figure 1. The cubic mesophases exhibit in the low-angle $2° < 2\theta < 6°$ region up to nine narrow Bragg diffraction peaks that could be indexed to a $Ia\bar{3}d$ space group symmetry (Figure 1a−c). This indicates a high-quality gyroid pore organization with good periodicity and large coherence lengths. The diffraction patterns of these materials lacked high angle ($2\theta > 7°$) Bragg reflections, indicating a nonperiodic nature of the framework at the atomic level. In the case of *h*-C_nPyInSbSe (Figure 1d), three reflections (100), (110), and (200) could be indexed, representing a MCM-41 type *P6mm* symmetry. The indexing of all powder patterns in Figure 1 along with the corresponding unit cell parameters is given in Table 1.

The unit cell constant of *c*-C_nPyMSbSe is ∼83 Å when $n = 14$ and ∼92 Å when $n = 16$. Compared to the *c*-C_n-PyPtSnSe system whose unit cell parameters are 85.1 Å for *c*-C_{18}PyPtSnSe and 95.1 Å for *c*-C_{20}PyPtSnSe,[8] those of *c*-C_n-PyMSbSe are quite large given that the building clusters and the surfactant carbon chain length are smaller in this system. Nevertheless, the increment in the cell dimensions in *c*-C_n-PyMSbSe ($n = 14, 16$) are ∼10 Å per CH_2-CH_2 unit, very similar to that in the *c*-C_nPyPtSnSe system.

c-C_{16}PyInSbSe and *c*-C_{16}PyCdSbSe have very similar unit cell sizes, but *c*-C_{16}PyZnSbSe has a slightly smaller one, corresponding to the smaller size of zinc. However, when the surfactant carbon chain length was reduced from C16 to C14, there was almost no difference in the unit cell parameters between *c*-C_{14}PyZnSbSe and *c*-C_{14}PyCdSbSe. This could imply that this unit cell size is close to the lower limit possible for an ordered cubic inorganic framework to form. Consistent with this notion is that when $C_{12}Py^+$ was used, an ordered mesostructure could not be obtained.[16] XRD of the product showed two broad Bragg diffraction peaks, consistent with a disordered wormhole mesostructure. When the longer surfactants $C_{18}Py^+$ and $C_{20}Py^+$ were employed with the same synthesis procedure, the former gave an XRD pattern without high index Bragg reflections, and the (220)

(13) (a) Aitken, J. A.; Marking, G. A.; Evain, M.; Iordanidis, L.; Kanatzidis, M. G. *J. Solid State Chem.* **2000**, *153*, 158. (b) Kortüm, G. *Reflectance spectroscopy. Principles, Methods, Applications*; Springer: Berlin, 1969.

(14) Barton, T. J.; Bull, L. M.; Klemperer, W. G.; Loy, D. A.; McEnaney, B.; Misono, M.; Monson, P. A.; Pez, G.; Scherer, G. W.; Vartuli, J. C.; Yaghi, O. M. *Chem. Mater.* **1999**, *11*, 2633.

(15) Bonhomme, F.; Kanatzidis, M. G. *Chem. Mater.* **1998**, *10*, 1153.

(16) The product became black almost immediately after the M^{m+}/H_2O solution was mixed with the solution of $C_{12}Py/SbSe_4/H_2O$. Note that all the well-ordered cubic phases are red in color; see Table 2.

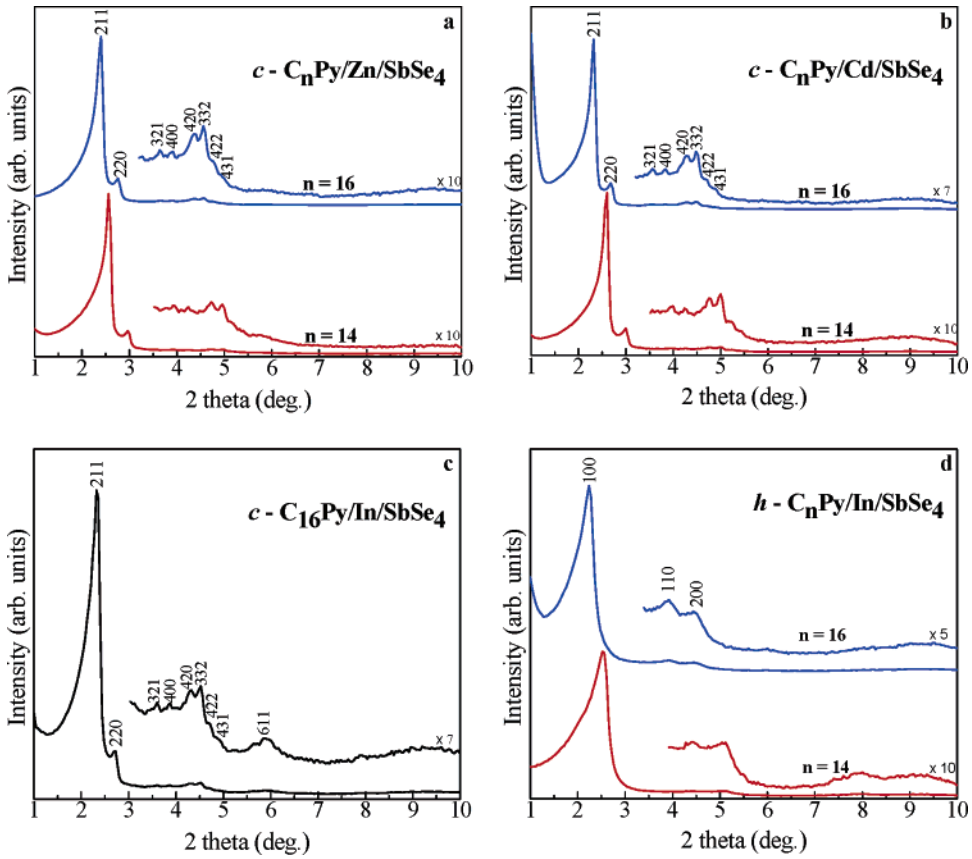

Figure 1. XRD patterns of (a) cubic zinc antimony selenides *c*-C_nPyZnSbSe; (b) cubic cadmium antimony selenides *c*-C_nPyCdSbSe; (c) cubic indium antimony selenide *c*-C_{16}PyInSbSe, and (d) hexagonal indium antimony selenides *h*-C_nPyInSbSe.

Table 1. Observed Bragg Reflections and Indexing for the Diffraction Patterns of Hexagonal/Cubic Metal Antimony Selenides

h-C_nPyInSbSe (*P6mm*)			*c*-C_nPyMSbSe (*Ia*$\bar{3}$*d*)					
	d (Å)			*d* (Å)				
				M = In^{3+}	M = Zn^{2+}		M = Cd^{2+}	
hkl	*n* = 14	n = 16	*hkl*	*n* = 16	*n* = 14	*n* = 16	*n* = 14	*n* = 16
100	35.3	39.4	211	37.7	34.2	36.8	34.1	37.9
110	20.1	22.6	220	32.7	29.6	31.9	29.5	32.8
200	17.3	19.8	321	24.5	22.4	24.3	22.1	24.8
			400	22.9	20.9	22.5	20.8	23.0
			420	20.5	18.6	20.3	18.5	20.6
			332	19.6	17.8	19.4	17.7	19.7
			422	18.8	17.1	18.4	17.0	18.8
			431	18.0		17.7	16.3	18.1
			611	14.9				
a (Å)	40.5 ± 2 0.3	45.5 ± 0.2	*a* (Å)	92.0 ± 0.3	83.5 ± 0.3	90.5 ± 0.5	83.1 ± 0.4	92.4 ± 0.4

peak became an ill-defined broad shoulder overlapping with the (211) peak; the longer $C_{20}Py^+$ gave a material with a clear lamellar diffraction pattern with only (001), (002), and (003) basal Bragg peaks. Similar trends were observed in the C_nPy/Pt/$SnSe_4$ system,[3b] in which the hexagonal mesostructure changed to lamellar when *n* was increased to 18. It is believed that the decrease in surface curvature as the carbon chain length increases causes the surfactant headgroups to pack more tightly and favor the lamellar packing.[3b]

TEM. The pore order and periodicity in the mesostuctures of *c*-C_nPyMSbSe and *h*-C_nPyInSbSe were observed directly by TEM. Typical TEM images of *c*-C_nPyMSbSe for M = Cd and M = Zn, respectively, are shown in Figure 2. For both cases, the pore order extends over a large area along with small regions of defects. The FFT (fast Fourier transform) patterns in the insets are consistent with the views along the [311] and [211] directions. Images and reciprocal space FT patterns such as these can only be obtained from objects of cubic symmetry, and they are fully consistent with the XRD patterns of Figure 1.

The typical TEM images of *h*-C_nPyInSbSe particles viewed parallel and perpendicular to the pore tunnels are shown in Figure 3a,b, respectively. The meso-scaled order can be seen to extend over all the particles which often tend to grow into hexagon-like shapes. However, there are also domains with less ordered pore arrangements which cause part of the edge of the particles to lose sharpness, Figure 3b. The estimated pore−pore separation and unit cell dimensions from the TEM experiments are in good agreement with those determined by XRD.

Table 2 summarizes some physical properties and elemental analysis results. Generally, in TGA experiments the

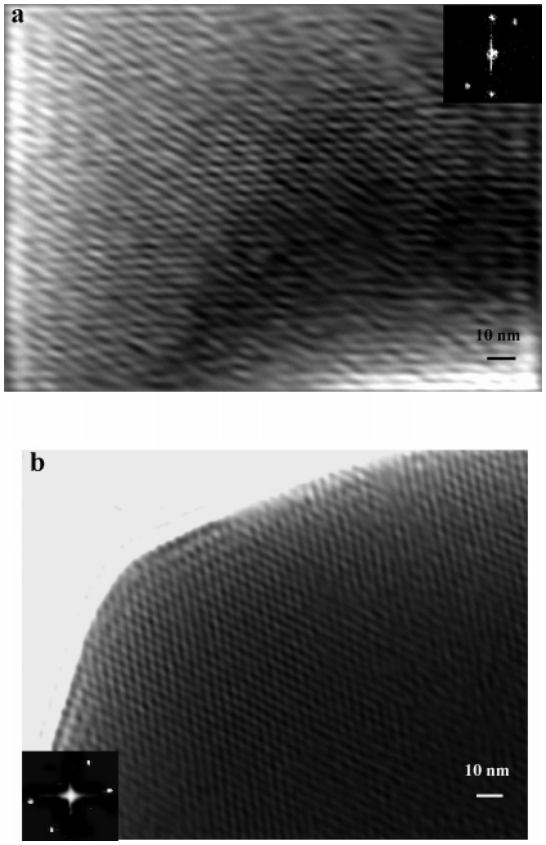

Figure 2. Representative TEM images of (a) *c*-C_{16}PyCdSbSe, view down the [311] axis, with the corresponding FFT pattern shown in the inset, and (b) *c*-C_{16}PyZnSbSe, view down the [211] axis, with the corresponding FFT pattern shown in the inset.

compounds showed no appreciable weight loss up to ~130 °C. In the case of cubic mesophases, a two-step weight loss generally occurred between 130 and 415 °C, which is evident from the slope change occurring at ~270 °C in the TGA curves. The weight loss of *c*-C_{16}PyInSbSe is relatively slower than the other cubic mesophases and ceases at ~508 °C (see Figure 4a). The color of the residue after TGA experiment was gray, and its powder XRD pattern comprised the crystalline binaries CdSe, CdSb, and Sb_2Se_3. The TGA curves of *h*-C_nPyInSbSe ($n = 14, 16$) are quite similar to that of the cubic ones, except that the slope change occurred at a slightly higher temperature at ~279 °C, Figure 4b. Like the other cluster-based mesostructured chalcogenides,[2−8] surfactant cations cannot be removed from the pores through thermal decomposition. This is because when the organic surfactants break up and leave the material as volatile species, they extract Se from the framework, causing its collapse. Pyrolysis mass spectra confirm the Se extraction when *c*-C_{16}PyCdSbSe is heated at 150 °C and 192 °C. The spectra showed a large peak with $m/z = 383.2$ and a minor one at $m/z = 606.4$, corresponding to the fragments $C_{16}H_{33}-Se_2$ and $(C_{16}H_{33})_2-Se_2$. Therefore, access to the pores has to be accomplished by other means such as ion-exchange processes (see below).

UV−Vis/Near-IR Spectroscopy. The optical absorption properties of *c*-C_nPyMSbSe and *h*-C_nPyInSbSe were investigated with solid-state UV−vis/near-IR spectroscopy. All solids possess well-defined optical absorptions associated with band gap transitions in the energy range 1.88−1.48 eV; see Table 2 and Figure 5. Generally, the energy gaps of these materials, though quite similar, do depend slightly on the carbon chain length. As pointed out previously,[3b] a mere replacement of one surfactant with another of a different chain length is expected to change the composition and local structure of the inorganic wall to some degree. This would cause small but real changes in the optical energy gap.[17] The band gap values are similar to most of the mesostructured selenides such as hexagonal[2,3b] and cubic[8] C_nPyPtSnSe as well as several useful semiconductors such as GaAs and CdSe. Therefore, it would be interesting to check if these materials have opto-electronic responses.

Time-Dependent Study on the Formation of the Cubic Mesostructure. To obtain a better insight as to how the cubic phase assembles and grows with time, the synthesis of *c*-C_{16}PyCdSbSe was observed under three different synthetic conditions. Namely, we examined (i) the product obtained instantly after all starting materials were mixed together; (ii) the product aged for ~18 h, and (iii) the product aged by stirring the reacting mixture for ~40 h. Figure 6 shows the powder XRD patterns and EDS results for each case. It is striking that the product obtained instantly already has the characteristics of cubic symmetry (as seen clearly by the presence of the (220) reflection), although the envelope of high index Bragg reflections is not so well-resolved. After aging for ~18 h, the cubic phase showed the sharpest and clearest Bragg reflections in the XRD pattern. After 40 h, however, the structural coherence of the pore order began to deteriorate as the reflections (211) and (220) began to overlap as a result of broadening. Meanwhile, the color evolved from orange (instant) to red (18 h) and finally brown (40 h). EDS analysis showed that the ratio of Se:Sb decreased from 4.0 (i) to 2.8 (iii) with prolonged aging. This could indicate a possible redox conversion of $[SbSe_4]^{3-}$ to $[SbSe_3]^{3-}$ with time (see below).

Raman Spectroscopy. To probe for the existence of the $[SbSe_4]^{3-}$ unit in the mesostructured materials, we studied their Raman spectra as well as those of the compounds K_3SbSe_4 and K_3SbSe_3. For *c*-C_{16}PyCdSbSe, at least four vibrational modes[18] were observed in the region of 100−600 cm^{-1} (Figure 7). The sharp peak centered at 209 cm^{-1} can be assigned to the totally symmetric ν_1 stretching mode of the $[SbSe_4]^{3-}$ cluster, corresponding to the 201 cm^{-1} peak in the spectrum of K_3SbSe_4 but slightly shifted due to coordination to the Cd^{2+} centers in the framework.[19,20] The peak at 175 cm^{-1} is absent in the spectrum of "free" $[SbSe_4]^{3-}$ or $[SbSe_3]^{3-}$ and could be assigned to a Cd−Se vibrational mode. The great broadening of this peak implies

(17) The effect the various types of organic templates have on the band gap may be understood in terms of variations in the chemical composition of the inorganic framework as a function of the surfactant chain length. In other words, the inorganic framework seems to adjust slightly its composition to respond to the changing micellar rod diameter, according to the demands imposed by the double point (2-WR) and triple point (3-WR) regions discussed in ref 3b.

(18) The vibrational modes were assigned referring to: Nakamoto, K. *Infrared and Raman Spectra of Inorganic and Coordination Compounds*, 5th ed.; Wiley: New York, 1997; Part A.

(19) The Raman peaks in the mesophases shifting slightly to higher energy compared to those in the starting free clusters were observed also in other mesostructured or 3D crystalline compounds synthesized from the same starting materials; see ref 5b.

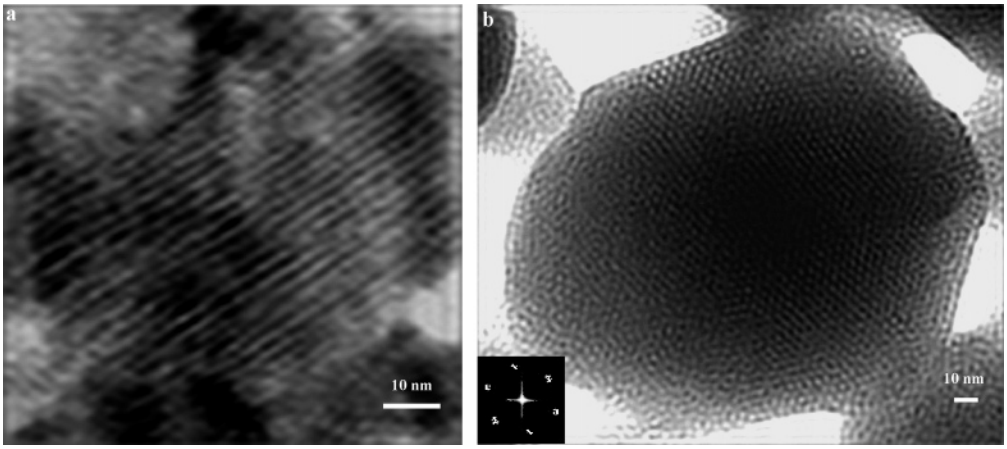

Figure 3. Representative TEM images of (a) *h*-C_{16}PyInSbSe, perpendicular to the pore tunnels, and (b) *h*-C_{16}PyInSbSe, parallel to the pore tunnels. The inset shows the corresponding FFT pattern which is consistent with hexagonal symmetry.

Table 2. Elemental Analysis and TGA,[a] Color, and Energy Gaps of C_nPyMSbSe Phases

mesophase	structure	C, H, N analyses (%)	atom ratio (M:Sb:Se)	TGA wt loss (%)	estimated formula[b] (calculated C, H, N%)	color	band gap (eV)
C_{14}Py/In/$SbSe_4$	hexagonal	21.89, 3.18, 1.21	0.66:1:4.1	41.8	$(C_{14}Py)_{2.7}In_{3.1}(SbSe_4)_4$ (21.60, 3.24, 1.33)	dark yellow	1.81
C_{16}Py/In/$SbSe_4$	hexagonal	29.14, 4.55, 1.68	0.70:1:3.7	45.5	$(C_{16}Py)_{2.7}In_{2.1}(SbSe_4)_{2.1}(SbSe_3)_{0.9}$ (29.53, 4.45, 1.64)	dark yellow	1.68
	cubic	28.28, 4.44, 1.51	0.60:1:3.4	44.0	$(C_{16}Py)_{2.4}In_{2.2}(SbSe_4)_{1.2}(SbSe_3)_{1.8}$ (28.09, 4.24, 1.56)	dark red	1.48
C_{14}Py/Zn/$SbSe_4$	cubic	30.80, 4.52, 1.81	0.85:1:3.8	50.0	$(C_{14}Py)_{5.2}Zn_{4.9}(SbSe_4)_4(SbSe_3)$ (30.68, 4.57, 1.88)	red	1.79
C_{16}Py/Zn/$SbSe_4$	cubic	33.98, 5.18, 1.80	0.80:1:3.4	52.8	$(C_{16}Py)_{5.2}Zn_{4.9}(SbSe_4)_2(SbSe_3)_3$ (34.01, 5.13, 1.89)	red	1.74
C_{14}Py/Cd/$SbSe_4$	cubic	30.76, 4.58, 1.81	0.77:1:4.1	49.7	$(C_{14}Py)_{5.8}Cd_{4.6}(SbSe_4)_5$ (30.71, 4.58, 1.89)	red	1.88
C_{16}Py/Cd/$SbSe_4$	cubic	33.96, 5.13, 1.80	0.75:1:4.0	53.9	$(C_{16}Py)_{6.2}Cd_{4.4}(SbSe_4)_5$ (34.21, 5.16, 1.90)	red	1.79

[a] The elemental compositions were determined by a combination of elemental C, H, and N analysis and energy-dispersive microprobe analysis (SEM/EDS, the metal ratios were calculated based on the average of ~10 measurements) results. [b] The formulae were estimated approximately based on the elemental analyses as well as the overall charge balance of the materials.

a wide distribution of Cd−Se bonding among the building blocks. The broad peak centered at 227 cm^{-1} could not be assigned to any $[SbSe_4]^{3-}$ mode. However, this feature corresponds to the 220 cm^{-1} shift observed in the spectrum of $[SbSe_3]^{3-}$, raising the possibility that in fact this unit is present in the framework. The broad Raman shift at 257 cm^{-1} can be assigned to the overlap of the ν_3 stretching mode of $[SbSe_4]^{3-}$ and ν_1 stretching mode of $[SbSe_3]^{3-}$ anions. These features are also observed (240 ~ 255 cm^{-1}) in the Raman spectra of K_3SbSe_4 and K_3SbSe_3.

To obtain further support of the existence of the $[SbSe_3]^{3-}$ in the cubic mesophases, Raman spectra of *c*-C_{16}PyZnSbSe and a product obtained from pure $[SbSe_3]^{3-}$ with In^{3+} under the same conditions (a disordered mesostructure, *w*-C_{16}PyInSbSe) were collected and compared with that of *c*-C_{16}PyCdSbSe; see Figure 8. The spectrum of *w*-C_{16}PyInSbSe lacked the peak centered at 209 cm^{-1}, confirming the absence of $[SbSe_4]^{3-}$, while both the 228 and 259 cm^{-1} peaks were present which can be assigned to the ν_3 and ν_1 modes of $[SbSe_3]^{3-}$. Because both these features are observed in the spectra of *c*-C_{16}PyCdSbSe and *c*-C_{16}PyZnSbSe, we conclude that an $Sb^{III}Se_3$ type fragment is probably present along with the original $[SbSe_4]^{3-}$ species in the gyroid structure.

According to the Raman spectrum, even the product obtained immediately upon reactant mixing already exhibits the shift at 227 cm^{-1}, suggesting rapid in situ formation of $[SbSe_3]^{3-}$ which must come from the reduction of K_3SbSe_4. Because the product obtained using $[SbSe_3]^{3-}$ as the precursor under the same conditions possesses a disordered mesostructure, we may conclude that the ordered *c*-C_nPyMSbSe probably requires both the tetrahedral $[SbSe_4]^{3-}$ and pyramidal $[SbSe_3]^{3-}$ units for its stability. The relative ratio of these two species in the structure might be controlled by factors such as structural requirements for cubic architecture, acidity of the starting mixture (caused by the Lewis acid center), size of the linking metal ions, surfactant carbon chain length, and aging period. It is possible that a fortuitous "perfect" mix of $[SbSe_4]^{3-}$/$[SbSe_3]^{3-}$ leads to the rapid formation of the ordered cubic structure at the preliminary stage of the reaction.

The formation of $[SbSe_3]^{3-}$ from $[SbSe_4]^{3-}$ is probably catalyzed by the Lewis acid centers Zn^{2+}, Cd^{2+}, and In^{3+}

(20) Another crystalline compound $Cs_3Ag_2Sb_3Se_8$, in which both $[SbSe_4]^{3-}$ and $[SbSe_3]^{3-}$ units were assembled in a one-dimensional ribbon, showed the ν_1 Raman shift of $[SbSe_4]^{3-}$ at 212 cm^{-1}. Hanko, J. A. Molten Salt Synthesis of Multinary Chalcoantimonates and Thiophosphates. Ph.D. Dissertation, Michigan State University, East Lansing, MI, 1998.

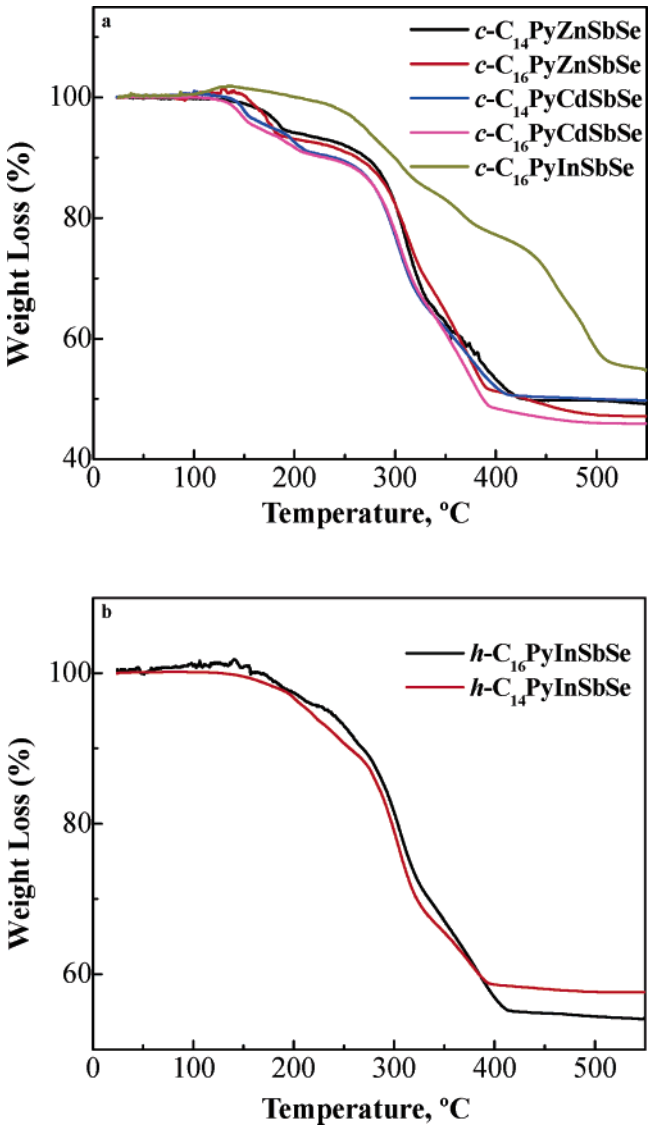

Figure 4. TGA curves of (a) *c*-C_nPyMSbSe (n = 14, 16; M = In, Zn, Cd) and (b) *h*-C_nPyInSbSe (n = 14, 16) materials under nitrogen flow (heating rate 10°/min).

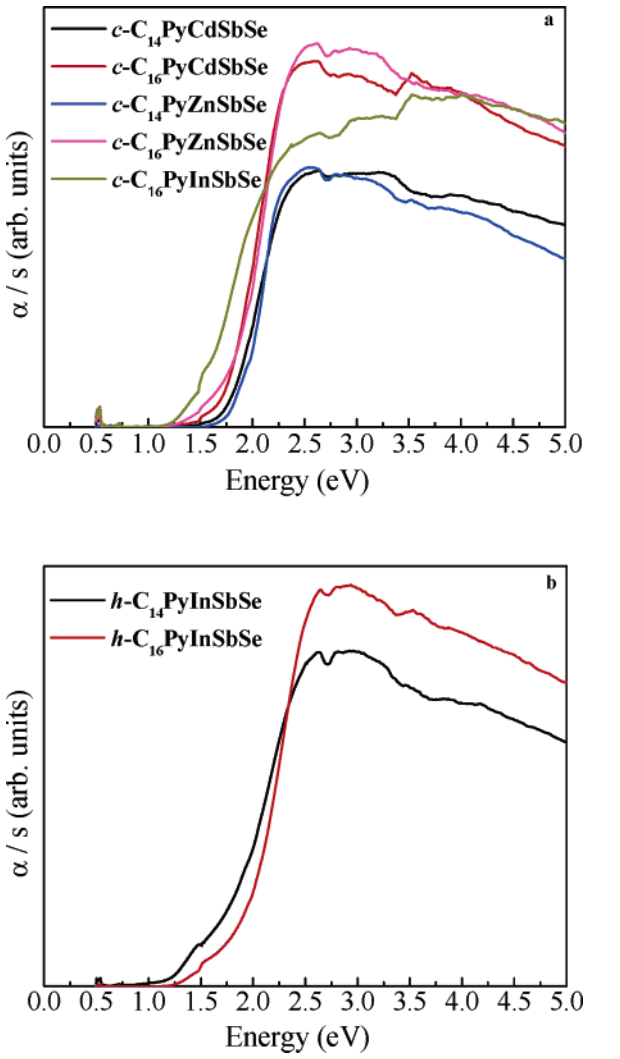

Figure 5. Solid-state UV−vis absorption spectra of (a) *c*-C_{16}PyMSbSe and (b) *h*-C_nPyInSbSe materials.

via an internal electron-transfer mechanism that reduces the Sb^{5+} center to Sb^{3+}. The stabilization of Sb^{5+} with Se^{2-} ligands very likely lies at the border of redox instability and requires a highly basic counterion (e.g., K_3SbSe_4). The replacement of the K^+ ions with more acidic Zn^{2+}, Cd^{2+}, and In^{3+} destabilizes the $Sb^{5+}-Se^{2-}$ combination in favor of $Sb^{3+}-Se_2^{2-}$. This is consistent with the absence of examples of $[SbSe_4]^{3-}$-containing compounds in which this anion is bound to divalent or trivalent metal centers. The Cu_3SbSe_4 and $Cs_3Ag_2(Sb_2Se_4)(SbSe_4)$[20] compounds are rare examples, and they involve monovalent Ag^+ and Cu^+ (i.e. the least Lewis basic) metal ions.

XANES Spectroscopy. The existence of the $[SbSe_4]^{3-}$ unit in the mesostructured materials was also investigated by XANES spectroscopy on the *c*-C_{16}PyZnSbSe, *c*-C_{16}PyCdSbSe, and *c*-C_{16}PyInSbSe phases as well as the reference compounds Cu_3SbSe_4 and Sb_2Se_3. Figure 9 shows the XANES spectra recorded at the Sb L_{III} edge for all compounds. The main absorption increase arises from $2p_{3/2} \rightarrow 5d$ transitions. In addition, there is a pre-edge peak in the spectra before the rising Sb L_{III} absorption edge, which is attributed to the transition from the $2p_{3/2}$ level toward the antibonding 5s σ^* level.[21,22] The intensity of the pre-edge peak depends

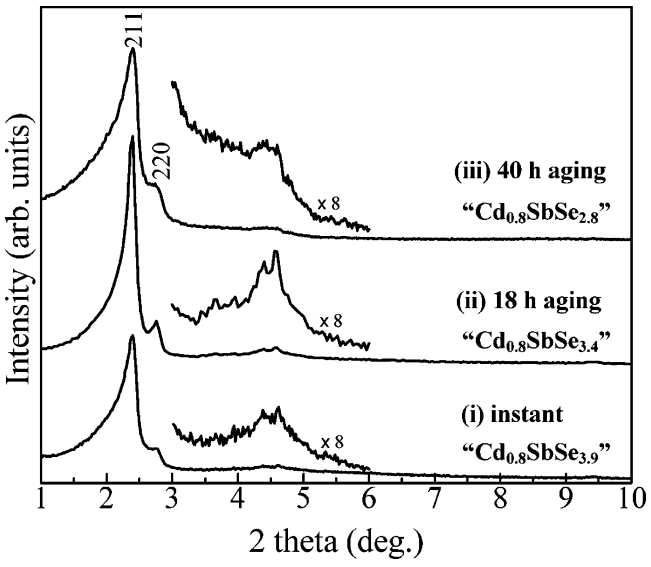

Figure 6. Powder XRD patterns of *c*-C_{16}PyCdSbSe formed in three different conditions: (i) product formed instantly through precipitation after all starting materials were mixed together; (ii) product aged for ~18 h; and (iii) product aged for ~40 h. The corresponding atomic ratios as obtained from EDS analysis results are shown.

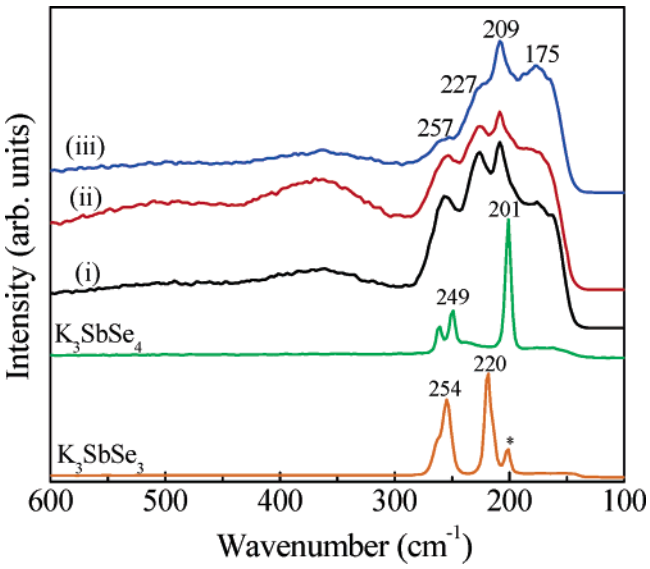

Figure 7. Raman spectra of *c*-C_{16}PyCdSbSe materials formed with three different time-dependent reactions of (i) instant and (ii) 18 h of aging and (iii) 40 h of aging during the synthesis along with the spectra of K_3SbSe_4 (green) and K_3SbSe_3 (orange). (*) The small peak at 201 cm^{-1} in the spectrum of K_3SbSe_3 is caused by a small amount of K_3SbSe_4 impurity.

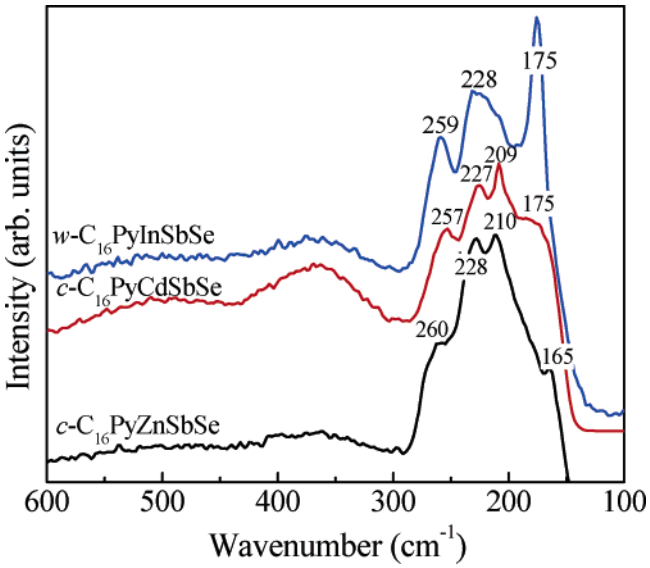

Figure 8. Raman spectra of *c*-C_{16}PyZnSbSe, *c*-C_{16}PyCdSbSe, and *w*-C_{16}PyInSbSe.

sensitively on the vacant density-of-states (dos) in the σ^*-derived band. In Sb(III) systems, the s^2 electron pair is stereochemically inactive, the pre-edge peak is typically of low intensity, and its magnitude correlates with the symmetry of the ligand polyhedron around the Sb(III) central atom. On the other hand, in Sb(V) compounds, the s^2 electrons participate fully in bonding with the surrounding ligands, and the increased vacant dos in the $5s\sigma^*$ band should lead to a more intense pre-edge feature. This is exactly what is observed experimentally (inset in Figure 9) for the reference compounds with the intensity significantly decreasing on going from Cu_3SbSe_4 ($[Sb^VSe_4]^{3-}$ units) to Sb_2Se_3 ($[Sb^{III}Se_3]^{3-}$

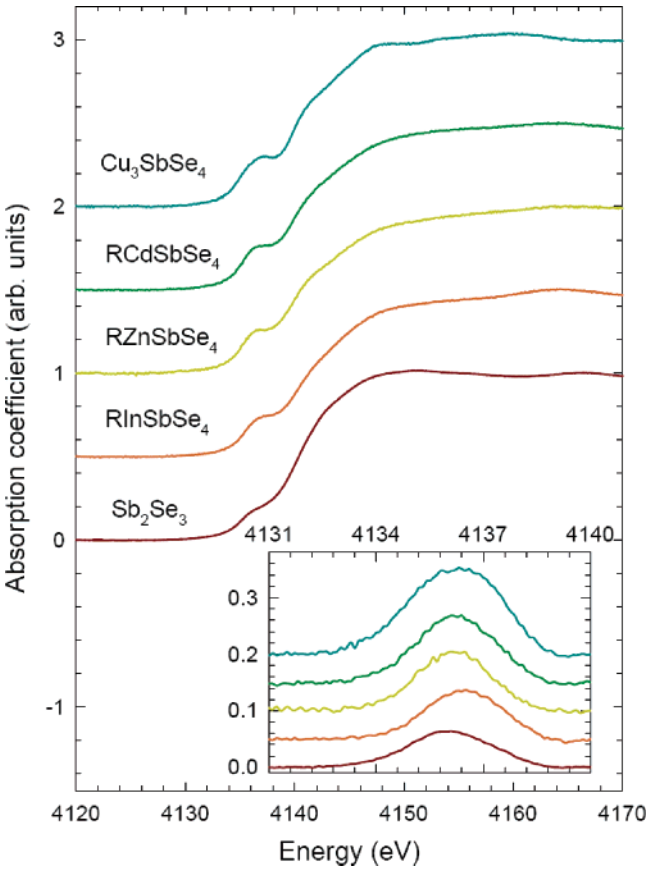

Figure 9. Ambient-temperature normalized XANES spectra at the Sb L_{III} edge of the cubic mesostructured phases, *c*-C_{16}PyCdSbSe, *c*-C_{16}PyZnSbSe, and *c*-C_{16}PyInSbSe, and the reference systems, Cu_3SbSe_4 and Sb_2Se_3. The spectra have been shifted upward for clarity. Inset: Normalized spectra in the vicinity of the pre-edge peak following subtraction of the rising absorption edge.

Table 3. Relative Intensities of the XANES Pre-Edge Peaks in the Cubic Mesostructured Phases, *c*-C_{16}PyCdSbSe, *c*-C_{16}PyZnSbSe, and *c*-C_{16}PyInSbSe, and the Reference Systems, Cu_3SbSe_4 and Sb_2Se_3

phase	relative intensity of pre-edge peak
Cu_3SbSe_4	100
c-C_{16}PyCdSbSe	65
c-C_{16}PyZnSbSe	57
c-C_{16}PyInSbSe	46
Sb_2Se_3	38

units). Furthermore, the integrated area of the pre-edge peak smoothly decreases from a value near that of Cu_3SbSe_4 to values near that of Sb_2Se_3 as we move along from *c*-C_{16}PyCdSbSe and *c*-C_{16}PyZnSbSe to the *c*-C_{16}PyInSbSe mesostructured phase (inset in Figure 9 and Table 3). This evolution is consistent with an increased proportion of the reduced $[Sb^{III}Se_3]^{3-}$ species at the expense of $[Sb^VSe_4]^{3-}$ as the Lewis acidity of the metal ions increases along the series Cd^{2+}, Zn^{2+}, and In^{3+} and is in agreement with the Raman spectroscopic results described earlier. Therefore, combined with elemental analysis results, the estimated formulae of these mesophases are given in Table 2 with both the $[Sb^VSe_4]^{3-}$ and $[Sb^{III}Se_3]^{3-}$ units. However, it should also be noticed that even in the cases of *h*-C_{14}PyInSbSe and *c*-C_nPyCdSbSe ($n = 14, 16$) only $SbSe_4$ was given, and it is quite possible that $[SbSe_3]^{3-}$ is part of the building block and the released Se^{2-} still exists in the framework; thus, the EDS ratio of Sb:Se remains 1:4.

(21) Durand, J.-M.; Lippens, P. E.; Olivier-Fourcade, J.; Jumas, J.-C.; Womes, M. *J. Non-Cryst. Solids* **1996**, *194*, 109.
(22) Nalin, M.; Messaddeq, Y.; Ribeiro, S. J. L.; Poulain, M.; Briois, V.; Brunklaus, G.; Rosenhahn, C.; Mosel, B. D.; Eckert, H. *J. Mater. Chem.* **2004**, *14*, 3398.

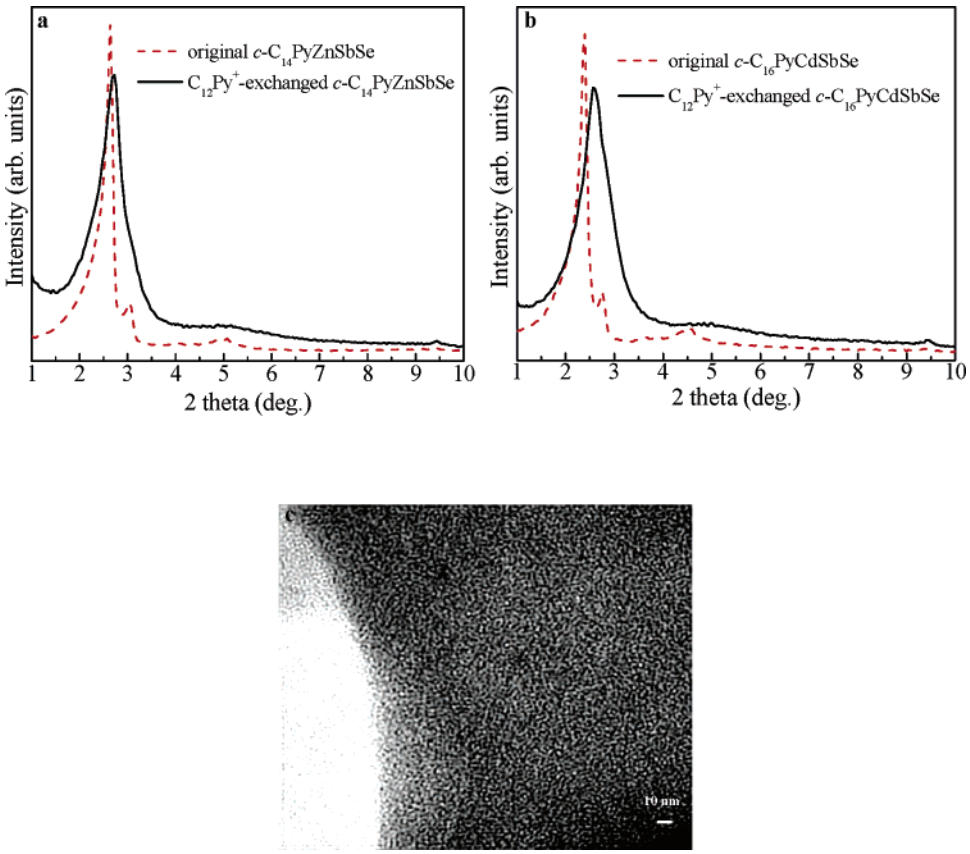

Figure 10. (a) XRD patterns of $C_{12}Py^+$-exchanged *c*-C_{14}PyZnSbSe (solid) and the original *c*-C_{14}PyZnSbSe (dashed); (b) XRD patterns of $C_{12}Py^+$-exchanged *c*-C_{16}PyCdSbSe (solid) and the original *c*-C_{16}PyCdSbSe (dashed); (c) TEM image of the $C_{12}Py^+$-exchanged *c*-C_{14}PyZnSbSe showing a disordered wormhole mesostructure.

Access to the Pores through Ion Exchange. The accessibility of the pore space in these materials was probed by investigating their ability to exchange the cation surfactants for other cationic species. Because cubic mesophases could not be obtained with $C_{12}Py^+$ directly under the same conditions, ion-exchange experiments of *c*-C_nPyMSbSe (M = Zn, Cd; n = 14, 16) with C_{12}PyBr were performed. Unlike the *c*-C_nPyPtSnSe materials which show an elastic inorganic framework[8,23] that can undergo ion exchange and adjust its pore diameter to the surfactant chain length by "shrinking", the framework in *c*-C_nPyMSbSe appears to be more rigid and selective to the carbon chain length. Figure 10 shows the XRD patterns before and after the ion-exchange reactions of C_{12}PyBr with *c*-C_{14}PyZnSbSe (10a) and *c*-C_{16}PyCdSbSe (10b), respectively. In both cases, the clear characteristics of the MCM-48 type mesostructure disappeared. The original (211) reflection and the other high index Bragg peaks coalesced into two broad features.

The *d* spacing of the main Bragg diffraction peak in Figure 10a shifts slightly from 33.34 Å (*c*-C_{14}PyZnSbSe) to 32.36 Å ($C_{12}Py^+$-exchanged *c*-C_{14}PyZnSbSe, C_{12}Py/C_{14}PyZnSbSe). Pyrolysis mass spectroscopy of C_{12}Py/C_{14}PyZnSbSe showed a major peak with m/z 248.3 (corresponding to fragment $C_{12}H_{25}Se$) and a small one with m/z = 276.3 (corresponding to fragment $C_{14}H_{29}Se$), indicating indeed that $C_{14}Py^+$ was substantially replaced by $C_{12}Py^+$ in *c*-C_{14}PyZnSbSe.

(23) Samkharadze, M.; Gigauri, R. I.; Ugulava, M.; Gigauri, R. D. *Bull. Georgian Acad. Sci.* **1999**, *159*, 74.

Table 4. Elemental Analysis of $C_{12}Py^+$-Exchanged Mesophases of *c*-C_nPyMSbSe (n = 14, 16; M = Zn, Cd)

mesophase	C, H, N analyses (%)
original *c*-C_{14}PyZnSbSe$_4$	34.21, 5.00, 2.04
$C_{12}Py^+$-exchanged C_{14}PyZnSbSe$_4$	28.90, 4.21, 1.82
original *c*-C_{16}PyCdSbSe$_4$	35.03, 5.34, 1.83
$C_{12}Py^+$-exchanged C_{16}PyCdSbSe$_4$	23.68, 3.26, 1.46

The *d* spacing of the main Bragg diffraction peak in Figure 10b shifts from 37.28 Å (*c*-C_{16}PyCdSbSe) to 34.11 Å ($C_{12}Py^+$-exhcanged *c*-C_{16}PyCdSbSe, C_{12}Py/C_{16}PyCdSbSe). Pyrolysis mass spectroscopy of C_{12}Py/C_{16}PyCdSbSe showed a large peak with m/z = 248.3 and only a trace of $C_{16}H_{33}Se$ (m/z = 304.3) was observed, again confirming that almost all $C_{16}Py^+$ was replaced with $C_{12}Py^+$. The corresponding C, H, and N analysis results are listed in Table 4 and are consistent with complete ion exchange.

The lower efficiency of the C_{12}Py-exchange reaction with *c*-C_{14}PyZnSbSe could imply that its unit cell size is close to the lower limit for an ordered cubic inorganic framework to be stable and, therefore, has stronger interaction with the supporting surfactant cations. Representative TEM images indicate that a disordered wormhole mesostructure was produced after ion exchange, Figure 10c.

Although the cubic symmetry in this system could not be retained, this framework showed reversible ion-exchange capacity. The product of the $C_{12}Py^+$-exchanged *c*-C_nPyMSbSe could be re-exchanged with other C_nPy^+ ions. (Supporting Information: Figure 1Sa shows the XRD pattern of $C_{16}Py^+$-exchanged C_{12}Py/C_{14}PyZnSbSe from Figure 10a (*r*-C_{16}Py/C_{12}Py/C_{14}PyZnSbSe). The *d* spacing of the main

Bragg diffraction peak shifts from 32.36 Å to 40.90 Å which is even larger than the *d* spacing of the (211) reflection of a pristine *c*-C_{16}PyZnSbSe material and suggests an expansion of the volume of the material. Both the C, H, and N analysis (gave a formula of $C_{21.5}H_{39.5}N$) and pyrolysis mass spectroscopy confirmed that the exchange was complete.

Interestingly, ion-exchange capacity was also observed with the hexagonal *h*-C_nPyInSbSe material. Figure 1Sb shows the powder XRD patterns of the original *h*-C_{16}PyInSbSe and $C_{12}Py^+$-exchanged (C_{12}Py/C_{16}PyInSbSe) and the reversed $C_{16}Py^+$-exchanged (*r*-C_{16}Py/C_{12}Py/C_{16}PyInSbSe) products. From *h*-C_{16}PyInSbSe to C_{12}Py/C_{16}PyInSbSe, the *d* spacing of the main Bragg diffraction peak in Figure 11b shifted from 38.75 Å to 37.28 Å. Pyrolysis mass spectroscopy of the $C_{12}Py^+$-exchanged material showed a large peak at $m/z = 248.3$ ($C_{12}H_{25}Se$) and a small one at $m/z = 304.3$ ($C_{16}H_{33}Se$), confirming the presence of $C_{12}Py^+$ in the pores. The reverse exchange from C_{12}PyInSbSe to *r*-C_{16}Py/C_{12}Py/C_{16}PyInSbSe caused the *d* spacing of the main Bragg diffraction peak to shift form 37.28 Å to 41.9 Å, which is in fact larger than that of the original *h*-C_{16}PyInSbSe. The main diffraction peaks broaden significantly, indicating a reduced coherence domain size and increased disorder. Pyrolysis mass spectroscopy of *r*-C_{16}Py/C_{12}Py/C_{16}PyInSbSe showed a large peak of $C_{16}H_{33}Se$ and only a trace of the peak corresponding to $C_{12}H_{25}Se$, confirming that almost all the $C_{12}Py^+$ ions were exchanged back to $C_{16}Py^+$. To the best of our knowledge, this may be the first example of reversible ion-exchange capacity of a hexagonal chalcogenide mesophase.

Concluding Remarks

The tetrahedral cluster $[SbSe_4]^{3-}$ and In^{3+}, Zn^{2+} and Cd^{2+} metal ions can combine in the presence of long chain surfactant cations to assemble a new group of semiconducting open-framework mesostructured phases with hexagonal and cubic symmetry. The cubic phases possess MCM-48 type gyroid surface and considerably expand the current small family of cubic mesostructured materials. Despite the rapid formation of these materials compared to the mesostructured silicas, the products possess surprisingly good nanoscale order.

Unlike MCM-48 silica, which is stabilized primarily through the organization of the surfactant under the proper temperature/concentration condition, the chalcogenide systems described here also need the "proper" inorganic fragments to provide a structural connectivity that is compatible with the formation of the gyroid surface. Apparently the highly restricted parameter space needed to build this structure is met in this case, judging from the facile synthesis of the gyroid surface $Ia\bar{3}d$ mesostructure from tetrahedral M^{2+} and $[SbSe_4]^{3-}$ precursors. This is in contrast to the silica MCM-48 which has a single inorganic building block and relies only on surfactant organization which can render it prone to reproducibility problems.[24]

Both the *c*-C_nPyMSbSe and *h*-C_nPyInSbSe exhibit reversible ion-exchange capability. The cubic and hexagonal symmetry of the mesostructures, however, could not be retained after the ion-exchange, and a disordered wormhole arrangement was produced. A key question emerging from this and previous work on mesostructures with cubic symmetry is this: what is the dominant factor controlling the assembly of the gyroid surface? Is it the surfactant size, shape, and concentration (as it seems increasingly likely) or the type of inorganic building unit and its coordination geometry? In silicas it is probably the former, but in chalcogenides it may be the latter or more likely a combination of both. Although the previous work on the Pt^{2+}/$[SnSe_4]^{4-}$,[3b] Pt^{2+}/$[Sn_4Se_{10}]^{4-}$,[2] and Pt^{2+}/$[Sn_2Se_6]^{4-}$ [8,24] systems provided clues as to the importance of building unit in structure selection (e.g., only the Pt^{2+}/$[Sn_2Se_6]^{4-}$ pair can give a cubic structure), the results reported here on a completely different anion provide additional insights on this key question. Because *c*-C_nPyMSbSe and *c*-C_nPyPtSnSe are based on building blocks with very different geometries, we may conclude that the cubic symmetry of the inorganic gyroid framework might be more accommodating in its constituents than previously thought. Therefore, we can expect the family of nonoxidic materials with cubic $Ia\bar{3}d$ mesostructures to grow as this fascinating structure can be accessible by a wider variety of building blocks.

Acknowledgment. This research was supported by NSF Grant CHE-0211029. This work made use of the SEM and TEM facilities of the Center for Advanced Microscopy at MSU. The authors thank the ESRF for the provision of synchrotron X-ray beam time.

Supporting Information Available: XRD patterns of the $C_{16}Py^+$-exchanged product from Figure 9a and of the original *h*-C_{16}PyInSbSe, C_{12}Py/C_{16}PyInSbSe, and reversed *r*-C_{16}Py/C_{12}Py/C_{16}PyInSbSe (PDF). This material is available free of charge via the Internet at http://pubs.acs.org.

CM0609956

(24) Trikalitis, P. N.; Ding, N.; Malliakas, C.; Billinge, S. J. L.; Kanatzidis, M. G. *J. Am. Chem. Soc.* **2004**, *126*, 15326.